

# UC San Diego

## UC San Diego Previously Published Works

### Title

Printable, high-performance solid-state electrolyte films

### Permalink

<https://escholarship.org/uc/item/90n7w051>

### Journal

Science Advances, 6(47)

### ISSN

2375-2548

### Authors

Ping, Weiwei  
Wang, Chengwei  
Wang, Ruiliu  
et al.

### Publication Date

2020-11-20

### DOI

10.1126/sciadv.abc8641

Peer reviewed

## MATERIALS SCIENCE

## Printable, high-performance solid-state electrolyte films

Weiwei Ping<sup>1\*</sup>, Chengwei Wang<sup>1\*</sup>, Ruiliu Wang<sup>1\*</sup>, Qi Dong<sup>1</sup>, Zhiwei Lin<sup>1</sup>, Alexandra H. Brozena<sup>1</sup>, Jiaqi Dai<sup>1</sup>, Jian Luo<sup>2</sup>, Liangbing Hu<sup>1†</sup>

Current ceramic solid-state electrolyte (SSE) films have low ionic conductivities ( $10^{-8}$  to  $10^{-5}$  S/cm), attributed to the amorphous structure or volatile Li loss. Herein, we report a solution-based printing process followed by rapid ( $\sim 3$  s) high-temperature ( $\sim 1500^\circ\text{C}$ ) reactive sintering for the fabrication of high-performance ceramic SSE films. The SSEs exhibit a dense, uniform structure and a superior ionic conductivity of up to 1 mS/cm. Furthermore, the fabrication time from precursor to final product is typically  $\sim 5$  min, 10 to 100 times faster than conventional SSE syntheses. This printing and rapid sintering process also allows the layer-by-layer fabrication of multilayer structures without cross-contamination. As a proof of concept, we demonstrate a printed solid-state battery with conformal interfaces and excellent cycling stability. Our technique can be readily extended to other thin-film SSEs, which open previously unexplored opportunities in developing safe, high-performance solid-state batteries and other thin-film devices.

## INTRODUCTION

The need for safer rechargeable batteries that avoid the use of flammable liquid organic electrolyte has motivated the development of solid-state electrolytes (SSEs) (1–3), such as lithium phosphorus oxynitride (LiPON) (4, 5) and garnet-based ceramic compounds (5–7). SSE films ( $< 10\ \mu\text{m}$ ) that feature a high ionic conductivity of  $> 10^{-4}$  S/cm are typically necessary to achieve high energy and power densities. However, current methods of producing such SSE films have notable challenges. For example, the vacuum-based radio frequency (RF) sputtering process used to deposit LiPON in batteries is cost prohibitive (8–10), limiting its broad applications. Similarly, other vacuum-based techniques used to fabricate various ceramic SSE films, such as atomic layer deposition (ALD) (11–13), pulsed layer deposition (PLD) (14, 15), and chemical vapor deposition (CVD) (16, 17), are more time-consuming and less scalable compared to the roll-to-roll process. Furthermore, ceramic SSEs produced by these methods generally exhibit low ionic conductivities of  $\sim 10^{-8}$  to  $10^{-4}$  S/cm (17–19) due to the amorphous structure deposited or high loss of volatile ions (e.g., Li and Na).

To address these limitations, more cost-effective and scalable solution-based methods have been developed to synthesize ceramic SSE films (e.g., garnet), but with limited success due to the tremendous challenges in sintering electrolyte films (11, 20, 21). In those processes, the SSEs need to be sintered at high temperatures ( $600^\circ$  to  $1100^\circ\text{C}$ ) for hours to achieve the crystalline structure necessary for a high ionic conductivity. However, prolonged sintering also causes severe Li and Na loss and corresponding low ionic conductivities due to the volatility of these light elements at high temperature (22–25). As a result, ceramic SSE films generally display either poor crystallinity or notable Li loss, with a maximum reported ionic conductivity of  $\sim 10^{-6}$  S/cm (26, 27). Lowering the processing temperature to prevent severe Li loss (2) or adding excess Li to compensate (11) has been a common strategy in traditional ceramic film deposition techniques. However, this leads to poor compositional control and

potentially a porous structure. In addition, these low-temperature sintered SSEs have an amorphous structure, leading to a limited conductivity improvement of up to  $2.9 \times 10^{-5}$  S/cm (2), which is far from the bulk value ( $\sim 10^{-3}$  S/cm) (28). While solid-state film batteries with a low current density of 50 to  $800\ \mu\text{A}/\text{cm}^2$  have been successfully commercialized in electronics (17, 29), it is impossible to translate this success to large-scale applications (e.g., electric vehicles) that require a current density of up to 3 to  $10\ \text{mA}/\text{cm}^2$  (30). As a result, there is a continuing need for a scalable method of synthesizing ceramic SSEs featuring excellent compositional control and crystallinity to achieve the necessary high ionic conductivities.

In this work, we developed a counterintuitive approach of synthesizing ceramic SSE films directly from the precursors, in which we greatly increase the sintering temperature (up to  $1500^\circ\text{C}$ ) but only for a short period of time ( $\sim 3$  s). This rapid heating enables the formation of a dense, polycrystalline film structure but with negligible volatile element loss due to the short sintering time. We call this method “printing and radiative heating” (PRH), a solution-based and printable technique for synthesizing ceramic SSE films. In a typical process, a precursor film is printed on a substrate with a thickness precisely tuned by controlling the ink concentration and wet thickness. The air-dried precursor film is then placed in close contact to a radiative heating strip (typically  $\sim 1500^\circ\text{C}$ ) for rapid close-proximity sintering (Fig. 1A). This Joule-heated strip runs across the precursor film with a gap of  $\sim 0.5$  mm and a total heating duration of a few seconds to complete the sintering process, potentially enabling roll-to-roll processing. Figure 1B and fig. S1 show a typical PRH-sintered  $\text{Li}_{6.5}\text{La}_3\text{Zr}_{1.5}\text{Ta}_{0.5}\text{O}_{12}$  (LLZTO) ceramic SSE film on a single-crystal MgO substrate, which features a translucent and dense structure with a surface roughness of  $< 1\ \mu\text{m}$  (Fig. 1C). The technique is also material nonspecific, with the ability to sinter a range of high-performance solid-state films.

## RESULTS AND DISCUSSION

To demonstrate the PRH method, we synthesized a ceramic LLZTO SSE film (see the Supplementary Materials for details). Briefly, we mixed the precursor powder ( $\text{Li}_2\text{CO}_3$ ,  $\text{La}_2\text{O}_3$ ,  $\text{ZrO}_2$ , and  $\text{Ta}_2\text{O}_5$ ) by ball milling, followed by dispersion in ethanol via sonication to prepare the precursor ink (Fig. 2A). The LLZTO precursor ink shows

Copyright © 2020 The Authors, some rights reserved; exclusive licensee American Association for the Advancement of Science. No claim to original U.S. Government Works. Distributed under a Creative Commons Attribution NonCommercial License 4.0 (CC BY-NC).

<sup>1</sup>Department of Materials Science and Engineering, University of Maryland, College Park, MD 20742, USA. <sup>2</sup>Department of NanoEngineering, Program of Materials Science and Engineering, University of California, San Diego, La Jolla, CA 92093, USA.

\*These authors contributed equally to this work.

†Corresponding author. Email: binghu@umd.edu

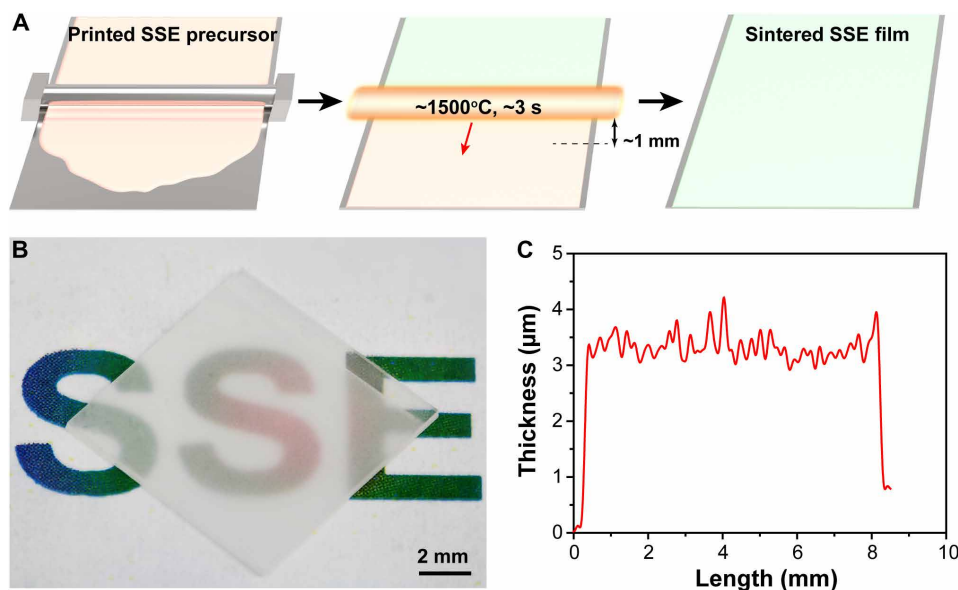


**Fig. 1. PRH process for film synthesis.** (A) Schematic of the film printing technique, which uses a ceramic precursor ink and a rapid sintering process that heats the material to high temperature ( $1500^{\circ}\text{C}$ ) within  $\sim 3$  s. (B) The sintered LLZTO garnet film on a single-crystal MgO substrate. (C) The corresponding profilometry curve of the sintered film. Photo credit: Weiwei Ping, University of Maryland, College Park.

good fluidity and wettability on various substrates (Fig. 2B), such as glass, metal foil, and ceramics, enabling multifunctional device engineering. In addition, the concentration and viscosity of the precursor ink can be modified for adaptation to different printing techniques, such as spray coating and the doctor blade method. We used spray coating to deposit the precursor ink to (i) achieve a wide range of thicknesses of the sintered LLZTO films (1 to  $100\ \mu\text{m}$ ) and (ii) create patterned films using a shadow mask, which enables the generation of various electrolyte and electrode structures for future device manufacturing (Fig. 2C and fig. S2). For nonpatterned and thicker films, we applied the doctor blade method to coat the precursor slurry on a metal foil (30 cm by 10 cm) in ambient environment (Fig. 2D), generating a smooth and uniform film (Fig. 2E and fig. S3).

In a typical PRH process, we rapidly sintered the printed precursor film in argon atmosphere by moving a Joule-heated carbon strip across the sample with a duration of  $\sim 3$  s (fig. S4). To demonstrate a large film on metal substrates, we fabricated a flexible LLZTO/LiBO<sub>2</sub> composite film on a stainless steel foil with size of 5 cm by 2 cm (fig. S5, A and B). LiBO<sub>2</sub> [30 weight % (wt %)] was added to decrease the sintering temperature of the composite SSE film so that the stainless steel substrate will not melt. The surface of LLZTO/LiBO<sub>2</sub> film remained conformal and flat without any obvious cracks or pinholes upon sintering, demonstrating excellent uniformity of the fabricated large SSE film (fig. S5, C to E). We studied the effect of the sintering temperature and time on the resulting LLZTO films using scanning electron microscopy (SEM) and x-ray diffraction (XRD). For a lower sintering temperature ( $\sim 1000^{\circ}\text{C}$ ), the resulting film has pure garnet phase (fig. S6) but with porous structure even with a longer sintering time of 10 s (Fig. 2F). For a higher sintering temperature ( $\sim 1700^{\circ}\text{C}$ ), the sintered film features abnormal grain growth (Fig. 2H), severe Li loss (fig. S6), and side reaction with the substrate (fig. S7), even when the sintering time is limited to just 1 s. However, we found that an optimized combination of high temperature and short processing time ( $1500^{\circ}\text{C}$ , 3 s) was able to achieve a dense garnet structure with minimum Li loss and side reactions (Fig. 2G and fig. S6).

To better understand the evolution of the LLZTO precursor film during PRH sintering, we sintered the films at temperatures ranging from  $\sim 800^{\circ}$  to  $1700^{\circ}\text{C}$  and times from 1 to 180 s. We measured the XRD patterns of the sintered films to characterize the potential phase changes associated with Li loss (Fig. 2I). According to the XRD patterns, the precursors start to react and form cubic garnet phase at low temperatures of  $800^{\circ}$  to  $1000^{\circ}\text{C}$  in  $\sim 30$  s. However, we observed that the low-temperature sintered films remained opaque white, indicating a porous structure, which we also confirmed by SEM (fig. S8). The porous garnet structure was maintained even when we increased the temperature up to  $\sim 1200^{\circ}\text{C}$  and the sintering time as long as 180 s, where slight Li loss was also observed from the appearance of a small La<sub>2</sub>Zr<sub>2</sub>O<sub>7</sub> peak (Fig. 2I). However, when the temperature was increased to  $1300^{\circ}$  to  $1500^{\circ}\text{C}$ , the printed precursor films became transparent, indicating a dense structure. As we increased the temperature further, the Li evaporation rate also increased rapidly, as demonstrated by the notable phase change to La<sub>2</sub>Zr<sub>2</sub>O<sub>7</sub> due to the severe Li loss (Fig. 2, I and J).

On the basis of additional sintering experiments and XRD studies, we constructed a quasi-time-temperature-transformation (TTT) diagram to determine the optimal sintering conditions to guide future synthesis (fig. S9). There are four main regions on the quasi-TTT diagram, indicating different densities and phases of the sintered LLZTO films. According to the quasi-TTT diagram, 3- to 10-s sintering at  $1300^{\circ}$  to  $1500^{\circ}\text{C}$  is preferred to achieve a robust film with minimum Li loss and dense structure. When the sintering temperature is lower than  $1200^{\circ}\text{C}$ , a long sintering time is required to achieve a dense film structure. However, the increased Li loss during such long sintering will result in the formation of La<sub>2</sub>Zr<sub>2</sub>O<sub>7</sub> phase, particularly for garnet films, due to the low starting Li content and shorter diffusion distances. Therefore, the sintering temperature and time must be well optimized to achieve a dense SSE film with pure garnet phase and minimum Li loss.

As the cross-sectional SEM image shows (Fig. 3A), a high temperature of  $1500^{\circ}\text{C}$  can provide enough energy to sinter the LLZTO

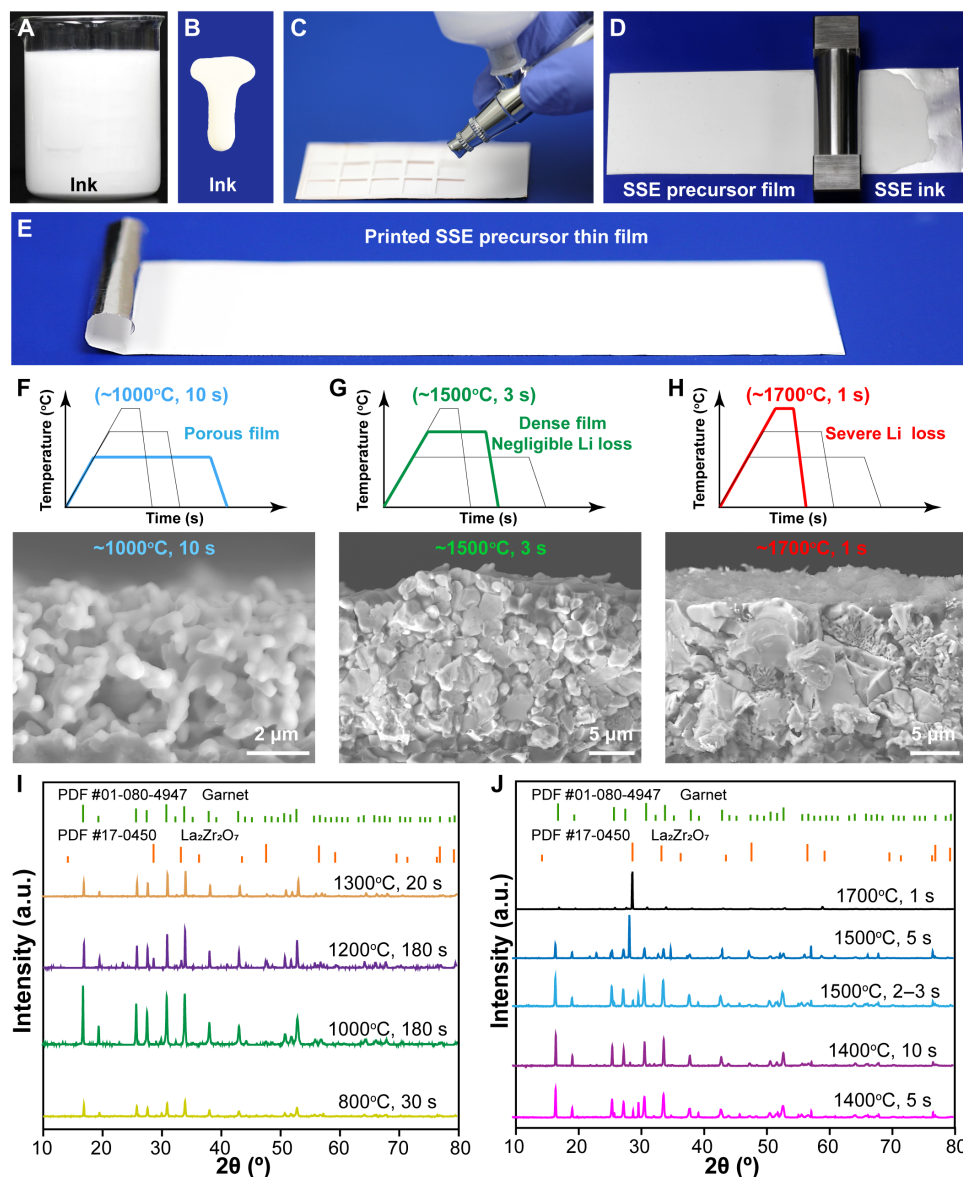


**Fig. 2. Optimization of ceramic film printing and sintering conditions.** (A) SSE precursor ink prepared by dispersing the mixed oxide precursors ( $\text{Li}_2\text{CO}_3$ ,  $\text{La}_2\text{O}_3$ ,  $\text{ZrO}_2$ , and  $\text{Ta}_2\text{O}_5$ ) in ethanol. (B) The SSE ink shows good fluidity. (C) Printing the garnet precursor ink by spray coating through a mask. (D) Printing the SSE precursor ink by the doctor blade method. (E) The printed SSE film is scalable and flexible. (F to H) Schematic and cross-sectional morphology of LLZTO garnet films sintered at different temperatures and times, in which an adequate sintering temperature with appropriate sintering time is necessary to acquire a dense garnet film with limited Li loss and uniform grain size distribution. XRD patterns of LLZTO films sintered at temperatures ranging from (I) 800° to 1300°C and hold times ranging from 1 to 180 s and at (J) 1400° to 1700°C and hold times ranging from 1 to 10 s. a.u., arbitrary units. Photo credit: Weiwei Ping, University of Maryland, College Park.

film and lead to a uniform structure without obvious pores (fig. S10, A and B). Even with a thickness as low as  $\sim 1.5 \mu\text{m}$ , the film still has a dense structure with no obvious pinholes in the fractured surface (fig. S10C). The XRD pattern of the LLZTO film also matches the standard cubic garnet phase (PDF #01-080-4947; fig. S10D), indicating minimum Li loss. In addition, in traditional sintering methods,  $\text{Al}_2\text{O}_3$  can become easily doped into garnet-based SSEs during sintering process (31, 32), which can affect the ionic conductivity and chemical stability of SSEs. The cross-sectional energy-dispersive x-ray spectroscopy (EDS) mapping of the PRH-sintered LLZTO (Fig. 3B) exhibits a clear interface with the  $\text{Al}_2\text{O}_3$  substrate, confirming no obvious crossover doping between the LLZTO film and

substrate. The absence of cross-doping further demonstrates the advantage of the combined high temperature and short sintering time made possible by the PRH technique. In addition, the rapid sintering process prevents abnormal grain growth at high temperature, as demonstrated by the uniform grain size distribution ( $\sim 1.6 \pm 0.7 \mu\text{m}$ ) from the top view SEM images (Fig. 3, C and D).

We evaluated the ionic conductivity of the PRH-sintered LLZTO garnet films by electrochemical impedance spectroscopy (EIS) at temperatures ranging from 30° to 140°C (fig. S11) using in-plane Li electrodes (fig. S12). The activation energy of Li transport fitted by the Arrhenius behavior of the Li-ion conductivity was 0.34 eV (Fig. 3E), similar to that of bulk garnet, while the ionic conductivity

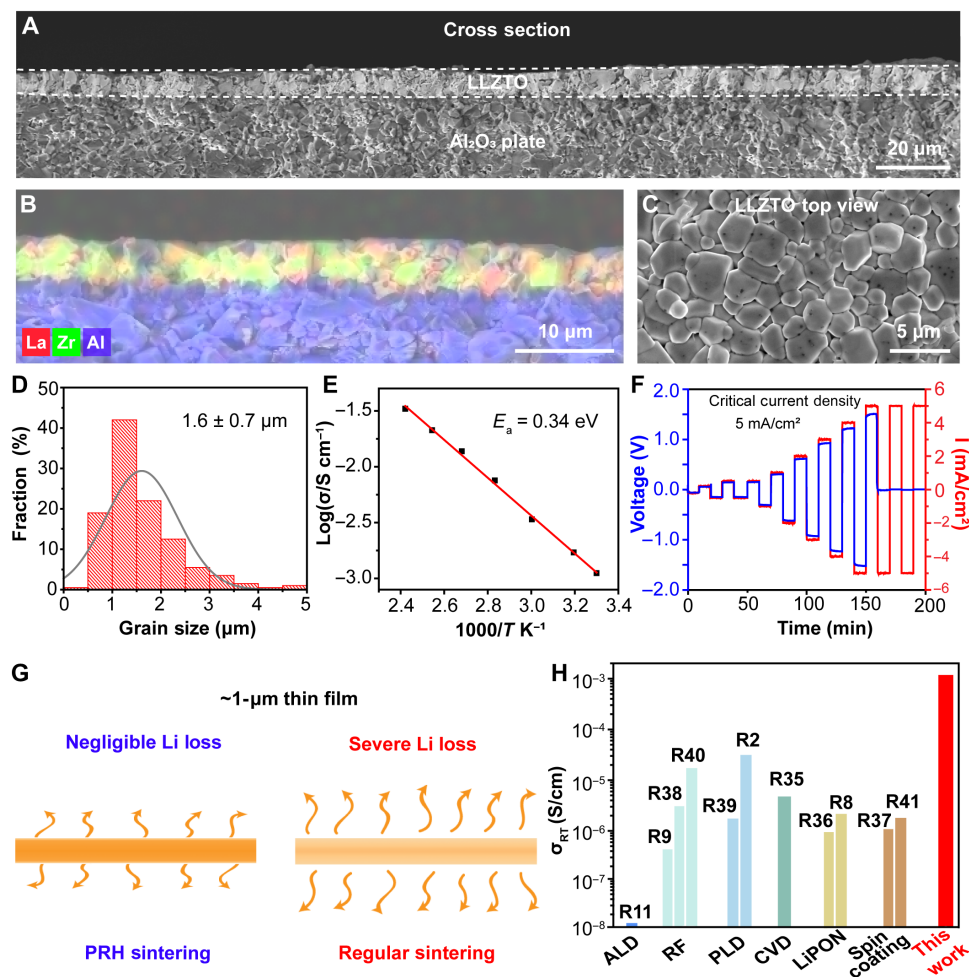


**Fig. 3. Performance of PRH-sintered LLZTO film.** (A) Cross-sectional SEM image and (B) EDS mapping of the sintered LLZTO film on an  $\text{Al}_2\text{O}_3$  substrate. (C) Surface morphology of the sintered LLZTO film on the  $\text{Al}_2\text{O}_3$  substrate. (D) Statistics of the grain size distribution of the sintered LLZTO film. (E) Activation energy of the PRH-sintered LLZTO film, fitted to an Arrhenius relationship. (F) Voltage and current profiles of the symmetric Li/LLZTO/Li cell with in-plane Li electrodes for critical current density test. (G) Comparison of Li loss in films sintered by PRH and conventional methods. (H) Comparison of the ionic conductivity at room temperature of SSE films synthesized by the PRH method and other reported techniques (2, 8, 9, 11, 35–41).

at room temperature was as high as  $\sim 1.0 \times 10^{-3}$  S/cm, which is comparable to that of bulk garnet (23, 33). We also evaluated the critical current density of the LLZTO film by conducting in-plane Li plating/stripping of a Li/LLZTO film/Li symmetric cell. The symmetric cell was cycled at current densities from 0.2 to 5 mA/cm<sup>2</sup> with the duration of 10 min (Fig. 3F). The PRH-sintered LLZTO film exhibited a critical current density of 5 mA/cm<sup>2</sup> (Fig. 3F and fig. S12), which is among the highest reported values, even for bulk garnet SSEs (28, 34). To better characterize the cycling stability of the PRH-sintered LLZTO film, a long-term cycling test was also performed for the Li/LLZTO film/Li symmetric cell (figs. S13 and S14). The Li/LLZTO film/Li symmetric cell can successfully cycle for more than 140 hours at current densities from 0.2 to 3 mA/cm<sup>2</sup>, indicating the excellent cycling stability of the PRH-sintered LLZTO film.

We attribute the excellent electrochemical properties of the PRH-sintered LLZTO films to the strong Li content control, dense morphology, and high crystallinity that are achieved during the extreme high-temperature and ultrafast sintering process. In contrast, conventional sintering processes normally take hours at  $>1000^\circ\text{C}$ ,

which leads to severe Li loss. This is particularly true for films (e.g.,  $\sim 1$  μm thick) compared to a regular thick pellet (e.g.,  $\sim 1000$  μm), as the amount of Li is much lower while the specific surface area is much higher, resulting in greater Li loss in conventional sintering processes (Fig. 3G). However, the rapid speed of the PRH method limits Li loss in such film structures, enabling us to achieve a LLZTO garnet film that exhibits the highest ionic conductivity among thin-film SSEs (Fig. 3H) (2, 8, 9, 11, 35–41).

The PRH sintering method is based on radiative heating, which is not material specific and can be applied to sinter a wide range of compositions. To demonstrate the universality of this technique, we successfully fabricated  $\text{Li}_{0.3}\text{La}_{0.567}\text{TiO}_3$  (LLTO),  $\text{Li}_{1.3}\text{Al}_{0.3}\text{Ti}_{1.7}(\text{PO}_4)_3$  (LATP), and  $\beta\text{-Al}_2\text{O}_3$  films from precursor ink solutions (Fig. 4A), all of which contain volatile components. LLTO, LATP, and  $\beta\text{-Al}_2\text{O}_3$  are high-performance Li-ion and Na-ion conductors whose films also face the challenge of controlling Li/Na loss during synthesis (19, 42, 43). In our method, we printed the LLTO, LATP, and  $\beta\text{-Al}_2\text{O}_3$  precursor inks on an  $\text{Al}_2\text{O}_3$  substrate by spray coating, followed by high-temperature ( $1500^\circ\text{C}$ ) sintering for  $\sim 3$  to 5 s, which

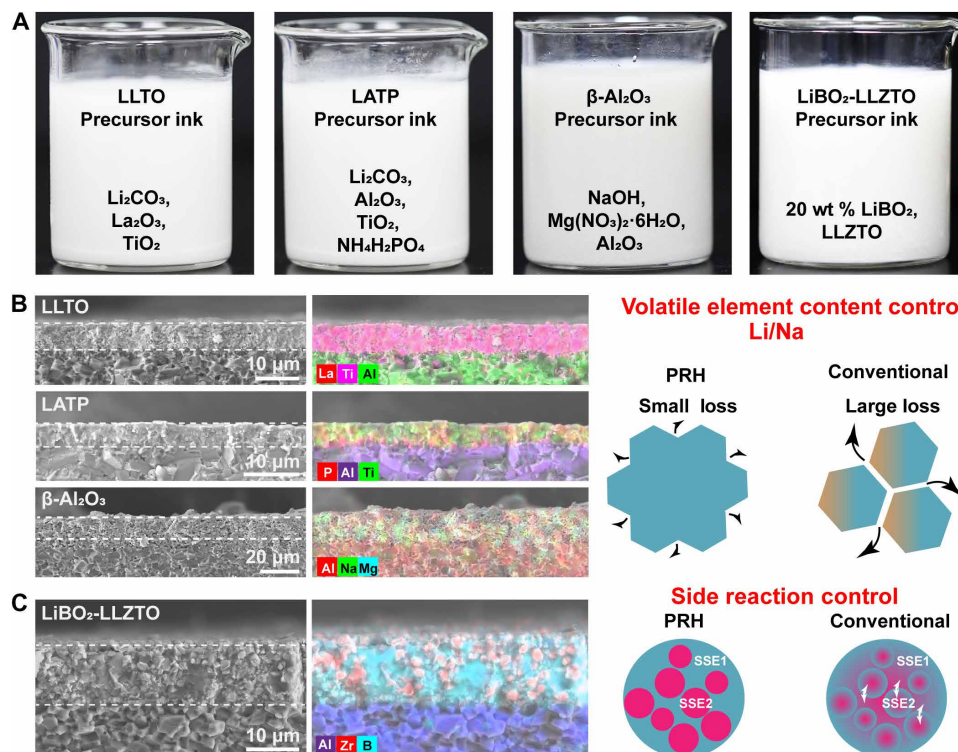


**Fig. 4. Other SSE films sintered by PRH.** (A) The printing inks of LLTO, LAMP,  $\beta$ -Al<sub>2</sub>O<sub>3</sub>, and LiBO<sub>2</sub>-LLZTO precursors. (B) Left: The cross-sectional morphology and elemental mapping results of the PRH-sintered LLTO, LAMP,  $\beta$ -Al<sub>2</sub>O<sub>3</sub> films. Right: Schematic of the volatile element loss comparison between PRH and conventional sintering methods. (C) Left: The cross-sectional morphology and mapping results of the PRH-sintered LiBO<sub>2</sub>-LLZTO film. Right: Schematic of the side reaction control comparison between PRH and conventional methods. Photo credit: Weiwei Ping, University of Maryland, College Park.

resulted in uniform and dense films with thicknesses of 5 to 10  $\mu\text{m}$  (Fig. 4B). The LAMP and LLTO films were sintered in air to prevent the potential reduction of Ti<sup>4+</sup>. Similar to the LLZTO film, no obvious cross-doping or side reactions between the SSE layer and substrate were observed, according to EDS mapping (Fig. 4B). The grain boundaries of the sintered films were also well merged because of the melting effect at high sintering temperature. Furthermore, because of the rapid sintering process within 3 s, the Li/Na loss in the LAMP, LLTO, and  $\beta$ -Al<sub>2</sub>O<sub>3</sub> SSEs was minimized, which we confirmed from the pure phases in the XRD patterns (figs. S15 to S17).

Besides single-component films, our PRH technique can also be used to rapidly sinter composite films, as the short sintering time can effectively prevent side reactions between materials. To demonstrate this ability, we sintered a LiBO<sub>2</sub>-LLZTO composite SSE film (Fig. 4, A and C). The resulting material featured LiBO<sub>2</sub> uniformly distributed between the LLZTO grains with conformal interfaces and no obvious co-doping, likely due to the short sintering time of 3 s, even with a high sintering temperature of 1200°C. In contrast, when we sintered the same materials in a conventional furnace for 1 hour, we obtained a porous structure with large reacted grains rather than a dense composite (fig. S18). Hour sintering in a conventional furnace leads to notable cross-diffusion and side reactions between components, while the PRH method is able to avoid such side reactions to generate composite structures (Fig. 4C, right). This ability to fabricate a broad range of both single-component and multicomponent compounds indicates the universality of our rapid printing and sintering process for manufacturing high-performance ceramic films.

The PRH technique can also be applied to fabricate solid-state batteries with layered structures via layer-by-layer printing and sintering. LiCoO<sub>2</sub> precursor solution (fig. S19) was printed on a thin, rapidly sintered LLZTO pellet, followed by PRH sintering at  $\sim 800^\circ\text{C}$  (due to the low reaction temperature) for  $\sim 3$  s to in situ synthesize the LiCoO<sub>2</sub> cathode. We then coated the Li metal anode on the other side of the pellet to form a LiCoO<sub>2</sub>/LLZTO/Li solid-state battery for cycling (Fig. 5A). Cross-sectional SEM imaging and EDS mapping (Fig. 5, B and C) indicate that the LiCoO<sub>2</sub> cathode was uniformly sintered on the LLZTO surface with a conformal and clear interface. The PRH-synthesized LiCoO<sub>2</sub> also shows XRD peaks well matching the standard LiCoO<sub>2</sub> phase without much secondary phase, indicating successful synthesis during the 3-s sintering time (fig. S20). Because of the high temperature and short sintering time, the sintered LiCoO<sub>2</sub> exhibits a nanoporous structure with a grain size of  $\sim 200$  nm (fig. S21) and a well-defined, conformal interface without obvious cross-doping with the LLZTO garnet (Fig. 5C). To facilitate Li transport in the porous LiCoO<sub>2</sub> layer and avoid capacity decay due to the volume change of the cathode during cycling, we used LiBO<sub>2</sub> as a solid-state binder mixed with the LiCoO<sub>2</sub> cathode (44). Because LiBO<sub>2</sub> can melt at  $\sim 850^\circ\text{C}$ , we directly printed and sintered the LiBO<sub>2</sub> precursor for 3 s into the porous LiCoO<sub>2</sub> layer using the PRH technique, which resulted in a uniform composite structure (Fig. 5, D and E). We then characterized the electrochemical performance of the resulting layer-by-layer printed and sintered all-solid-state LiBO<sub>2</sub>-LiCoO<sub>2</sub>/LLZTO/Li battery.

Because of the conformal interfaces, the interfacial resistance of this PRH-sintered battery was as low as  $\sim 100$  ohm·cm<sup>2</sup> at 60°C

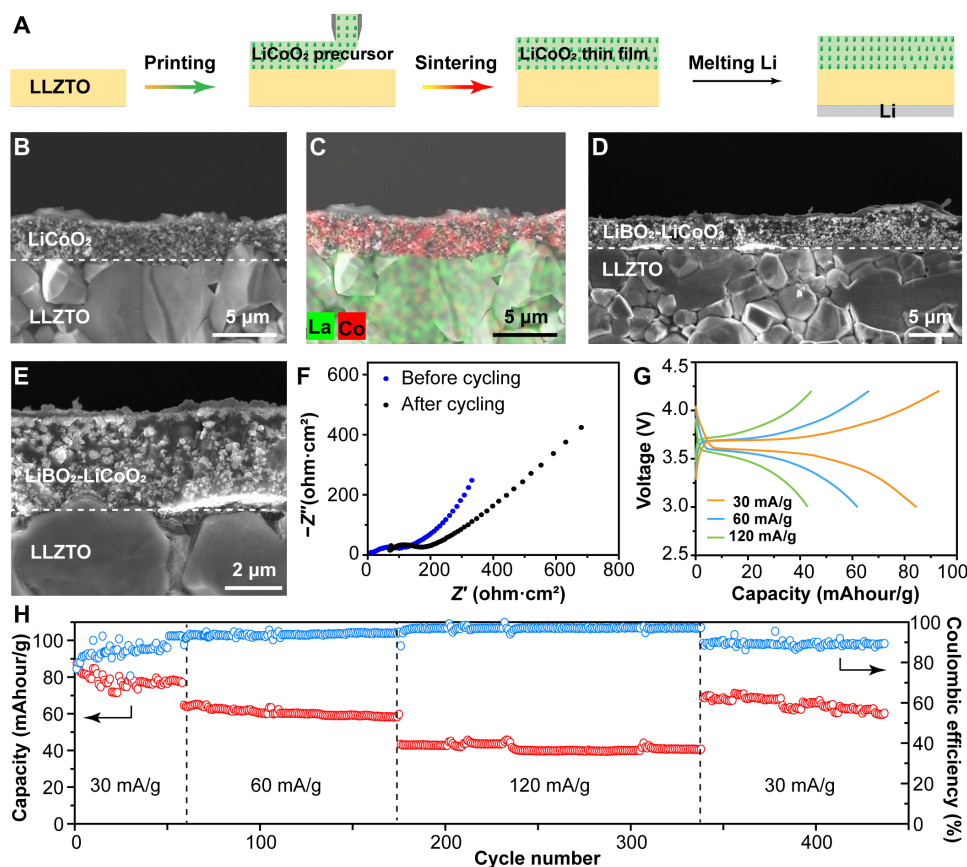


**Fig. 5. All-solid-state battery LiBO<sub>2</sub>-LiCoO<sub>2</sub>/LLZTO/Li sintered by PRH.** (A) The printing and sintering process of the PRH-fabricated solid-state battery. (B) Cross-sectional SEM image and (C) EDS mapping of the PRH-sintered LiCoO<sub>2</sub> cathode on the LLZTO surface. (D) Cross-sectional and (E) magnified SEM images of the LiBO<sub>2</sub>-LiCoO<sub>2</sub>/LLZTO interface. (F) EIS spectra of the all-solid-state battery (LiBO<sub>2</sub>-LiCoO<sub>2</sub>/LLZTO/Li) before cycling and after the 450<sup>th</sup> cycle. (G) Voltage profiles of the in situ fabricated all-solid-state battery at different current densities. (H) Cycling performance and Coulombic efficiency of the LiBO<sub>2</sub>-LiCoO<sub>2</sub>/LLZTO/Li all-solid-state battery at 60°C.

(Fig. 5F), which is considerably smaller than other co-sintered all-solid-state batteries (44–46). The voltage profiles of the printed battery exhibited typical plateaus of the LiCoO<sub>2</sub> cathode (Fig. 5G), further demonstrating the successful synthesis of LiCoO<sub>2</sub> via the rapid PRH technique. In addition, the battery's rate and cycling performance show good capacity retention and excellent cycling stability over ~450 cycles (Fig. 5H). Specifically, the initial specific capacity was ~87 mA-hour/g at a current density of 30 mA/g, which is better than most previous reports using co-sintered LiCoO<sub>2</sub> and garnet (37, 43, 44). The capacity slightly decreases with increasing current density but has little change over the cycles at each current density (Fig. 5H). After ~450 cycles, the interfacial resistance slightly increased to ~170 ohm-cm<sup>2</sup> (Fig. 5F), which further demonstrates the excellent stability of the in situ sintered cathode and interface synthesized by the PRH technique.

## Conclusion

In this work, we report a new technique for synthesizing ceramic SSE films that combines ink printing and high-temperature, close-proximity sintering. The LLZTO garnet electrolyte film displays a high Li ionic conductivity of up to 10<sup>-3</sup> S/cm, which is comparable to the garnet bulk. The high-temperature heating (up to 1500°C) at close proximity to the printed ceramic precursor ink completes the

sintering process in as little as 3 s, which effectively suppresses Li loss, thus overcoming a long-standing challenge of film sintering for compositions containing volatile elements. We extended this technique to multiple ceramic SSE films, including LATP, LLTO, β-Al<sub>2</sub>O<sub>3</sub>, and LiBO<sub>2</sub>-LLZTO, as well as thin-film cathode to demonstrate the versatility of our approach. Furthermore, we demonstrated the fabrication of multilayer structures by the PRH method in a layer-by-layer manner, with minimal interlayer cross-contamination/reactions. As a proof of concept, a layer-by-layer PRH-sintered solid-state battery was fabricated, which exhibited an excellent interface and stable cycling behavior. The PRH method allows us to produce ceramic films in a scalable manner with potential applications for next-generation batteries and thin-film devices.

## MATERIALS AND METHODS

### Fabrication of thin-film printable ink LLZTO printable ink

The LLZTO precursors, including Li<sub>2</sub>CO<sub>3</sub> (99.0%, Sigma-Aldrich), La<sub>2</sub>O<sub>3</sub> (99.0%, Sigma-Aldrich), ZrO<sub>2</sub> (99.0%, Sigma-Aldrich), and Ta<sub>2</sub>O<sub>5</sub> (99.0%, Sigma-Aldrich), were stoichiometrically mixed according to the formula of LLZTO, with 10 wt % excess Li<sub>2</sub>CO<sub>3</sub> added to compensate for the Li loss. After ball milling for 6 hours with

isopropanol and ZrO<sub>2</sub> balls, the LLZTO precursor powder was dried at 150°C for 20 min. During the drying process, the 150°C is just for vaporizing the solvent, not for the presintering the precursor. The LLZTO ink was then prepared by dispersing the LLZTO precursor powder in ethanol at a concentration of 20 mg/ml for spray printing and 600 mg/ml for doctor blade printing. The viscosity of the LLZTO precursor ink can be modified using polyvinyl pyrrolidone (PVP) at different concentrations for different printing methods. PVP (5 wt %) was added to the precursor powder for spray printing and doctor blade printing.

The thin LLZTO pellet used in all-solid-state batteries was fabricated by pressing the dried LLZTO precursor powder after ball milling. The precursor powder is pressed into disks under the pressure of 4.5 MPa uniaxially with diameter of 10 mm and thickness of 0.4 mm. The sample was sintered by ultrafast high-temperature sintering in inert atmosphere for 10 s.

#### **LATP printable ink**

The LATP precursors, including Li<sub>2</sub>CO<sub>3</sub> (99.0%, Sigma-Aldrich), Al<sub>2</sub>O<sub>3</sub> (99.0%, Sigma-Aldrich), TiO<sub>2</sub> (99.0%, Sigma-Aldrich), and NH<sub>4</sub>H<sub>2</sub>PO<sub>4</sub> (99.0%, Sigma-Aldrich), were stoichiometrically mixed according to the formula of LATP, with 10 wt % excess Li<sub>2</sub>CO<sub>3</sub> added to compensate for the Li loss. After ball milling for 6 hours with isopropanol, the LATP precursor powder was dried at 150°C for 20 min. After drying, the LATP precursor powder was then sintered for 30 min at 500°C to release the NH<sub>3</sub> and CO<sub>2</sub> from the raw materials. Then, the LATP precursor powder was dispersed in ethanol at a concentration of 20 mg/ml for spray printing. PVP (5 wt %) was added to the precursor powder for spray printing and doctor blade printing.

#### **LLTO printable ink**

The LLTO precursors, including Li<sub>2</sub>CO<sub>3</sub> (99.0%, Sigma-Aldrich), La<sub>2</sub>O<sub>3</sub> (99.0%, Sigma-Aldrich), and TiO<sub>2</sub> (99.0%, Sigma-Aldrich), were stoichiometrically mixed according to the formula of LLTO, with 10 wt % Li<sub>2</sub>CO<sub>3</sub> added to compensate for the Li loss. After ball milling for 6 hours with isopropanol, the LLTO precursor powder was dried at 150°C for 20 min and then dispersed in ethanol at a concentration of 20 mg/ml for spray printing. PVP (5 wt %) was added to the precursor powder for spray printing and doctor blade printing.

#### **LiCoO<sub>2</sub> printable ink**

The LiCoO<sub>2</sub> printable ink was prepared by stoichiometrically mixing LiNO<sub>3</sub> (99.0%, Sigma-Aldrich) and Co(NO<sub>3</sub>)<sub>2</sub>·6H<sub>2</sub>O (99.0%, Sigma-Aldrich). The mixed raw materials were then dispersed in ethanol at a concentration of 100 mg/ml for spray printing.

#### **Na<sub>2</sub>Mg<sub>0.67</sub>Al<sub>10.33</sub>O<sub>17</sub> (β-Al<sub>2</sub>O<sub>3</sub>) printable ink**

The β-Al<sub>2</sub>O<sub>3</sub> printable ink was prepared by mixing NaOH (99.0%, Sigma-Aldrich), Mg(NO<sub>3</sub>)<sub>2</sub>·6H<sub>2</sub>O (99.0%, Sigma-Aldrich), and Al<sub>2</sub>O<sub>3</sub> (99.0%, Sigma-Aldrich) according to the formula of Na<sub>2</sub>Mg<sub>0.67</sub>Al<sub>10.33</sub>O<sub>17</sub>, with 10% excess NaOH added to compensate for the Na loss. The mixed powders were then dispersed in ethanol at a concentration of 20 mg/ml. PVP (5 wt %) was added to the precursor powder for spray printing and doctor blade printing.

#### **LiBO<sub>2</sub>-LLZTO printable ink**

LiBO<sub>2</sub>-LLZTO ink was made by first mixing presintered LLZTO powder and 20 wt % LiBO<sub>2</sub> (99.9%, Sigma-Aldrich). The mixed compound was then dispersed in ethanol to form the precursor ink at a concentration of 20 mg/ml for spray printing. PVP (5 wt %) was added to the precursor powder for spray printing and doctor blade printing.

## **PRH method**

### **Printing process**

The doctor blade (VF1522, TQC Baker film applicator) method was used to print the precursor inks on different metal foil (Al, Cu, and stainless steel) and ceramic substrates (Al<sub>2</sub>O<sub>3</sub> and MgO) with a width of 10 cm and wet film thickness of 10 to 100 μm. To achieve micro- or nanoscale thin films, the spray printing technique was used to print the precursor film on Al or Cu foil, as well as ceramic substrates (MgO and Al<sub>2</sub>O<sub>3</sub>) at 60°C. The Dual Action Airbrush Kit with Mini Compressor (Point Zero) was used for spray printing. The gap between airbrush kit and substrate is about 1 to 2 cm. Single-crystal MgO was chosen for its transparency, which allowed us to visually monitor the sintering process as the opaque printed precursor inks turned translucent after Joule heating.

### **Rapid sintering process**

The heater was made of carbon felt (AvCarb Felt G200; ~10 cm in length, ~1 cm in width, and ~2 mm in thickness) purchased from the Fuel Cell Store, which we fixed on a glass plate by copper foil or silver paste (SPI Supplies). Two aluminum clips were attached to the carbon felt to connect it with a high-power dc source (Volteq HY6020EX) featuring a tunable current (0 to 20 A) and voltage (0 to 50 V). The Joule heating process was conducted in a glovebox with argon or air atmosphere on the basis of the requirement of the sample. The LLTO, LATP, LiCoO<sub>2</sub>, and LiBO<sub>2</sub>-LiCoO<sub>2</sub> thin films were sintered in air. LLZTO, β-Al<sub>2</sub>O<sub>3</sub>, and LiBO<sub>2</sub>-LLZTO thin films were sintered in argon. The typical sintering time for a small sample (~1 cm by 1 cm) was about 3 s. For a large sample, the heating strip moves slowly across the sample with a speed of ~1 cm/3 s.

### **Characterization**

The morphology and elemental mapping of the sample cross sections and surfaces were observed by SEM (Hitachi SU-70) coupled with an EDS detector. The phase structure of the thin films was characterized by XRD (Bruker D8 ADVANCE powder diffractometer) with a Cu Kα radiation source (λ = 1.54056 Å) at 40 kV and 40 mA. The temperature was characterized by fitting the curve of the ultraviolet-visible (UV-vis) spectra of the carbon felt heater using the Planck function (47). The UV-vis spectra were measured with a Vision Research Phantom Miro M110 high-speed camera.

### **Cell assembly and electrochemical performance tests**

For the Li/LLZTO film/Li symmetric cell, the in-plane Li metal electrodes were coated on the PRH-sintered LLZTO thin-film surface according to the method described in (48) (fig. S12).

The all-solid-state battery was fabricated by the PRH technique, in which the LiCoO<sub>2</sub> precursor ink was printed on the sintered LLZTO surface by spray printing and then sintered at 800°C for 3 s to form the LiCoO<sub>2</sub>/LLZTO thin film. As LiCoO<sub>2</sub> is known to experience volumetric change during cycling (44), we formed a composite by printing LiBO<sub>2</sub> on the LiCoO<sub>2</sub> cathode and sintering at ~1000°C for 3 s, which melts and infuses the LiBO<sub>2</sub> into the porous LiCoO<sub>2</sub> to improve the contact interface of LiCoO<sub>2</sub>/LLZTO. A thin carbon nanotube layer was coated on the sintered LiBO<sub>2</sub>-LiCoO<sub>2</sub> cathode to act as the current collector. After coating the Li metal (48) on the other side of the LLZTO, the all-solid-state battery was successfully fabricated with the structure of LiBO<sub>2</sub>-LiCoO<sub>2</sub>/LLZTO/Li.

EIS spectra of the symmetric Li/LLZTO film/Li cell were tested using a BioLogic MPG-2 battery cyler with a frequency range of 1 MHz to 500 mHz and temperature range of 30° to 140°C. The EIS of the LiBO<sub>2</sub>-LiCoO<sub>2</sub>/LLZTO/Li cell was tested in the same manner



but at 60°C. The galvanostatic charge/discharge of the all-solid-state LiBO<sub>2</sub>-LiCoO<sub>2</sub>/LLZTO/Li battery was performed at 60°C with current densities of 30, 60, and 120 mA/g without any organic electrolyte. The critical current density test of Li/LLZTO film/Li cell was performed at current densities from 0.2 to 5 mA/cm<sup>2</sup> with the Li plating/stripping duration of 10 min. Cycling performance of Li/LLZTO film/Li was performed at current densities from 0.2 to 3 mA/cm<sup>2</sup> for more than 140 hours. All batteries were tested in an argon-filled glove box. Note that the ionic conductivity of the specific film for critical current density and cycling test is about  $3 \times 10^{-4}$  and  $4 \times 10^{-4}$  S/cm, respectively. The slight variation of the ionic conductivity is due to the slight variation of the sintering temperature and time for different batches.

## SUPPLEMENTARY MATERIALS

Supplementary material for this article is available at <http://advances.sciencemag.org/cgi/content/full/6/47/eabc8641/DC1>

## REFERENCES AND NOTES

- L. Fan, S. Wei, S. Li, Q. Li, Y. Lu, Recent progress of the solid-state electrolytes for high-energy metal-based batteries. *Adv. Energy Mater.* **8**, 1702657 (2018).
- R. Pfenninger, M. Struzik, I. Garbayo, E. Stilp, J. L. M. Rupp, A low ride on processing temperature for fast lithium conduction in garnet solid-state battery films. *Nat. Energy* **4**, 475–483 (2019).
- J.-T. Han, Y.-H. Huang, J. B. Goodenough, New anode framework for rechargeable lithium batteries. *Chem. Mater.* **23**, 2027–2029 (2011).
- N. J. Dudney, Solid-state thin-film rechargeable batteries. *Mater. Sci. Eng. B* **116**, 245–249 (2005).
- P. Albertus, S. Babinec, S. Litzelman, A. Newman, Status and challenges in enabling the lithium metal electrode for high-energy and low-cost rechargeable batteries. *Nat. Energy* **3**, 16–21 (2018).
- J.-F. Wu, W. K. Pang, V. K. Peterson, L. Wei, X. Guo, Garnet-type fast Li-ion conductors with high ionic conductivities for all-solid-state batteries. *ACS Appl. Mater. Interfaces* **9**, 12461–12468 (2017).
- L. Porz, T. Swamy, B. W. Sheldon, D. Rettenwander, T. Frömling, H. L. Thaman, S. Berends, R. Uecker, W. C. Carter, Y.-M. Chiang, Mechanism of lithium metal penetration through inorganic solid electrolytes. *Adv. Energy Mater.* **7**, 1701003 (2017).
- J. B. Bates, N. J. Dudney, G. R. Gruzalski, R. A. Zuhr, A. Choudhury, C. F. Luck, J. D. Robertson, Electrical properties of amorphous lithium electrolyte thin films. *Solid State Ion.* **53–56**, 647–654 (1992).
- D. J. Kalita, S. H. Lee, K. S. Lee, D. H. Ko, Y. S. Yoon, Ionic conductivity properties of amorphous Li-La-Zr-O solid electrolyte for thin film batteries. *Solid State Ion.* **229**, 14–19 (2012).
- X. Yan, W. Han, Preparation and application of garnet electrolyte thin films: Promise and challenges. *Org. Chem. Plus* **1**, 6–22 (2020).
- E. Kazyak, K.-H. Chen, K. N. Wood, A. L. Davis, T. Thompson, A. R. Bielinski, A. J. Sanchez, X. Wang, C. Wang, J. Sakamoto, N. P. Dasgupta, Atomic layer deposition of the solid electrolyte garnet Li<sub>7</sub>La<sub>3</sub>Zr<sub>2</sub>O<sub>12</sub>. *Chem. Mater.* **29**, 3785–3792 (2017).
- E. Kazyak, K. N. Wood, N. P. Dasgupta, Improved cycle life and stability of lithium metal anodes through ultrathin atomic layer deposition surface treatments. *Chem. Mater.* **27**, 6457–6462 (2015).
- J. Xie, A. D. Sendek, E. D. Cubuk, X. Zhang, Z. Lu, Y. Gong, T. Wu, F. Shi, W. Liu, E. J. Reed, Y. Cui, Atomic layer deposition of stable LiAlF<sub>4</sub> lithium ion conductive interfacial layer for stable cathode cycling. *ACS Nano* **11**, 7019–7027 (2017).
- J. Tan, A. Tiwari, Fabrication and characterization of Li<sub>7</sub>La<sub>3</sub>Zr<sub>2</sub>O<sub>12</sub> thin films for lithium ion battery. *ECS Solid State Lett.* **1**, Q57–Q60 (2012).
- W. Jung, J. O. Dereux, W. C. Chueh, Y. Hao, S. M. Haile, High electrode activity of nanostructured, columnar ceria films for solid oxide fuel cells. *Energ. Environ. Sci.* **5**, 8682–8689 (2012).
- H. Ye, S. Xin, Y.-X. Yin, J.-Y. Li, Y.-G. Guo, L.-J. Wan, Stable Li plating/stripping electrochemistry realized by a hybrid Li reservoir in spherical carbon granules with 3D conducting skeletons. *J. Am. Chem. Soc.* **139**, 5916–5922 (2017).
- A. Patil, V. Patil, D. Wook Shin, J.-W. Choi, D.-S. Paik, S.-J. Yoon, Issue and challenges facing rechargeable thin film lithium batteries. *Mater. Res. Bull.* **43**, 1913–1942 (2008).
- I. Garbayo, M. Struzik, W. J. Bowman, R. Pfenninger, E. Stilp, J. L. M. Rupp, Glass-type polyamorphism in Li-garnet thin film solid state battery conductors. *Adv. Energy Mater.* **8**, 1702265 (2018).
- S. Wenzel, T. Leichtweiss, D. A. Weber, J. Sann, W. G. Zeier, J. Janek, Interfacial reactivity benchmarking of the sodium ion conductors Na<sub>3</sub>PS<sub>4</sub> and sodium β-alumina for protected sodium metal anodes and sodium all-solid-state batteries. *ACS Appl. Mater. Interfaces* **8**, 28216–28224 (2016).
- X. Yu, A. Manthiram, Enhanced interfacial stability of hybrid-electrolyte lithium-sulfur batteries with a layer of multifunctional polymer with intrinsic nanoporosity. *Adv. Funct. Mater.* **29**, 1805996 (2019).
- P. K. Arcot, J. Luo, Solution-based synthesis of oxide thin films via a layer-by-layer deposition method: Feasibility and a phenomenological film growth model. *Surf. Coat. Technol.* **202**, 2690–2697 (2008).
- A. Manthiram, X. Yu, S. Wang, Lithium battery chemistries enabled by solid-state electrolytes. *Nat. Rev. Mater.* **2**, 16103 (2017).
- A. Sharafi, E. Kazyak, A. L. Davis, S. Yu, T. Thompson, D. J. Siegel, N. P. Dasgupta, J. Sakamoto, Surface chemistry mechanism of ultra-low interfacial resistance in the solid-state electrolyte Li<sub>7</sub>La<sub>3</sub>Zr<sub>2</sub>O<sub>12</sub>. *Chem. Mater.* **29**, 7961–7968 (2017).
- K. Zhao, Y. Liu, S. Zhang, S. He, N. Zhang, J. Yang, Z. Zhan, A room temperature solid-state rechargeable sodium ion cell based on a ceramic Na-β'-Al<sub>2</sub>O<sub>3</sub> electrolyte and NaTi<sub>2</sub>(PO<sub>4</sub>)<sub>3</sub> cathode. *Electrochem. Commun.* **69**, 59–63 (2016).
- S. Wheeler, K. Hurlbutt, M. Pasta, A new solid-state sodium-metal battery. *Chem* **4**, 666–668 (2018).
- A. M. Nolan, Y. Liu, Y. Mo, Solid-state chemistries stable with high-energy cathodes for lithium-ion batteries. *ACS Energy Lett.* **4**, 2444–2451 (2019).
- V. Thangadurai, S. Narayanan, D. Pinzaru, Garnet-type solid-state fast Li-ion conductors for Li batteries: Critical review. *Chem. Soc. Rev.* **43**, 4714–4727 (2014).
- S. Teng, J. Tan, A. Tiwari, Recent developments in garnet based solid state electrolytes for thin film batteries. *Curr. Opin. Solid State Mater. Sci.* **18**, 29–38 (2014).
- Z. Tu, S. Choudhury, M. J. Zachman, S. Wei, K. Zhang, L. F. Kourkoutsis, L. A. Archer, Fast ion transport at solid-solid interfaces in hybrid lithium anodes. *Nat. Energy* **3**, 310–316 (2018).
- R. Murugan, V. Thangadurai, W. Weppner, Fast lithium ion conduction in garnet-type Li<sub>7</sub>La<sub>3</sub>Zr<sub>2</sub>O<sub>12</sub>. *Angew. Chem. Int. Ed.* **46**, 7778–7781 (2007).
- K. Liu, J.-T. Ma, C.-A. Wang, Excess lithium salt functions more than compensating for lithium loss when synthesizing Li<sub>6.5</sub>La<sub>3</sub>Ta<sub>0.5</sub>Zr<sub>1.5</sub>O<sub>12</sub> in alumina crucible. *J. Power Sources* **260**, 109–114 (2014).
- W. Xia, B. Xu, H. Duan, Y. Guo, H. Kang, H. Li, H. Liu, Ionic conductivity and air stability of Al-doped Li<sub>7</sub>La<sub>3</sub>Zr<sub>2</sub>O<sub>12</sub> sintered in alumina and Pt crucibles. *ACS Appl. Mater. Interfaces* **8**, 5335–5342 (2016).
- M. Bitzer, T. Van Gestel, S. Uhlenbruck, H.-P. Buchkremer, Sol-gel synthesis of thin solid Li<sub>7</sub>La<sub>3</sub>Zr<sub>2</sub>O<sub>12</sub> electrolyte films for Li-ion batteries. *Thin Solid Films* **615**, 128–134 (2016).
- X.-B. Cheng, R. Zhang, C.-Z. Zhao, Q. Zhang, Toward safe lithium metal anode in rechargeable batteries: A review. *Chem. Rev.* **117**, 10403–10473 (2017).
- C. Loho, R. Djenedic, M. Bruns, O. Clemens, H. Hahn, Garnet-type Li<sub>7</sub>La<sub>3</sub>Zr<sub>2</sub>O<sub>12</sub> solid electrolyte thin films grown by CO<sub>2</sub>-laser assisted CVD for all-solid-state batteries. *J. Electrochem. Soc.* **164**, A6131–A6139 (2017).
- J. Schwenzel, V. Thangadurai, W. Weppner, Developments of high-voltage all-solid-state thin-film lithium ion batteries. *J. Power Sources* **154**, 232–238 (2006).
- M. Zarabian, M. Bartolini, P. Pereira-Almao, V. Thangadurai, X-ray photoelectron spectroscopy and AC impedance spectroscopy studies of Li-La-Zr-O solid electrolyte thin film/LiCoO<sub>2</sub> cathode interface for all-solid-state Li batteries. *J. Electrochem. Soc.* **164**, A1133–A1139 (2017).
- J. Nong, H. Xu, Z. Yu, G. Zhu, A. Yu, Properties and preparation of Li-La-Ti-Zr-O thin film electrolyte. *Mater. Lett.* **154**, 167–169 (2015).
- J. S. Park, L. Cheng, V. Zorba, A. Mehta, J. Cabana, G. Chen, M. M. Doeff, T. J. Richardson, J. H. Park, J.-W. Son, W.-S. Hong, Effects of crystallinity and impurities on the electrical conductivity of Li-La-Zr-O thin films. *Thin Solid Films* **576**, 55–60 (2015).
- M. Rawlence, A. N. Filippin, A. Wäckerlin, T.-Y. Lin, E. Cuervo-Reyes, A. Remhof, C. Battaglia, J. L. M. Rupp, S. Buecheler, Effect of gallium substitution on lithium-ion conductivity and phase evolution in sputtered Li<sub>7-3x</sub>Ga<sub>x</sub>La<sub>3</sub>Zr<sub>2</sub>O<sub>12</sub> thin films. *ACS Appl. Mater. Interfaces* **10**, 13720–13728 (2018).
- R.-J. Chen, M. Huang, W.-Z. Huang, Y. Shen, Y.-H. Lin, C.-W. Nan, Sol-gel derived Li-La-Zr-O thin films as solid electrolytes for lithium-ion batteries. *J. Mater. Chem. A* **2**, 13277–13282 (2014).
- Z. Jiang, S. Wang, X. Chen, W. Yang, X. Yao, X. Hu, Q. Han, H. Wang, Tape-casting Li<sub>0.34</sub>La<sub>0.56</sub>TiO<sub>3</sub> ceramic electrolyte films permit high energy density of lithium-metal batteries. *Adv. Mater.* **32**, 1906221 (2019).
- H. S. Kim, Y. Oh, K. H. Kang, J. H. Kim, C. S. Yoon, Characterization of sputter-deposited LiCoO<sub>2</sub> thin film grown on NASICON-type electrolyte for application in all-solid-state rechargeable lithium battery. *ACS Appl. Mater. Interfaces* **9**, 16063–16070 (2017).
- K. Park, B.-C. Yu, J.-W. Jung, Y. Li, W. Zhou, H. Gao, S. Son, J. B. Goodenough, Electrochemical nature of the cathode interface for a solid-state lithium-ion battery: Interface between LiCoO<sub>2</sub> and garnet-Li<sub>7</sub>La<sub>3</sub>Zr<sub>2</sub>O<sub>12</sub>. *Chem. Mater.* **28**, 8051–8059 (2016).

45. T. Kato, T. Hamanaka, K. Yamamoto, T. Hirayama, F. Sagane, M. Motoyama, Y. Iriyama, In-situ  $\text{Li}_7\text{La}_3\text{Zr}_2\text{O}_{12}/\text{LiCoO}_2$  interface modification for advanced all-solid-state battery. *J. Power Sources* **260**, 292–298 (2014).
46. G. Vardar, W. J. Bowman, Q. Lu, J. Wang, R. J. Chater, A. Aguadero, R. Seibert, J. Terry, A. Hunt, I. Waluyo, D. D. Fong, A. Jarry, E. J. Crumlin, S. L. Hellstrom, Y.-M. Chiang, B. Yildiz, Structure, chemistry, and charge transfer resistance of the interface between  $\text{Li}_7\text{La}_3\text{Zr}_2\text{O}_{12}$  electrolyte and  $\text{LiCoO}_2$  cathode. *Chem. Mater.* **30**, 6259–6276 (2018).
47. M. Freitag, H.-Y. Chiu, M. Steiner, V. Perebeinos, P. Avouris, Thermal infrared emission from biased graphene. *Nat. Nanotechnol.* **5**, 497–501 (2010).
48. C. Wang, H. Xie, L. Zhang, Y. Gong, G. Pastel, J. Dai, B. Liu, E. D. Wachsman, L. Hu, Universal soldering of lithium and sodium alloys on various substrates for batteries. *Adv. Energy Mater.* **8**, 1701963 (2017).

**Acknowledgments:** We acknowledge the support of the Maryland Nanocenter, including its Surface Analysis Center and AIMLab. **Funding:** This project is not directly funded. **Author contributions:** L.H., C.W., and W.P. designed the experiments. W.P. and R.W. carried out the

experiments. Z.L. and J.D. created the three-dimensional illustrations. L.H., W.P., C.W., Q.D., A.H.B., and J.L. collectively wrote the paper. All authors commented on the final manuscript. **Competing interests:** The authors have applied for a provisional patent application through the University of Maryland (U.S. provisional patent 62/849578). The authors declare that they have no other competing interests. **Data and materials availability:** All data needed to evaluate the conclusions in the paper are present in the paper and/or the Supplementary Materials. Additional data related to this paper may be requested from the authors.

Submitted 22 May 2020

Accepted 5 October 2020

Published 18 November 2020

10.1126/sciadv.abc8641

**Citation:** W. Ping, C. Wang, R. Wang, Q. Dong, Z. Lin, A. H. Brozena, J. Dai, J. Luo, L. Hu, Printable, high-performance solid-state electrolyte films. *Sci. Adv.* **6**, eabc8641 (2020).